

<https://doi.org/10.1038/s43247-024-01282-1>

Northern Hemisphere winter atmospheric teleconnections are intensified by extratropical ocean-atmosphere coupling

Check for updates

Masato Mori ¹✉, Yu Kosaka ², Bunmei Taguchi ³, Hiroki Tokinaga ¹, Hiroaki Tatebe ⁴ & Hisashi Nakamura²

The role of extratropical atmosphere-ocean coupling in generating and maintaining large-scale atmospheric low-frequency variability remains an open question owing to vigorous atmospheric internal fluctuations. Here, we use coupled and uncoupled large-ensemble global model simulations to clarify how the coupling intensifies atmospheric teleconnection patterns in the Northern Hemisphere winter. We show that the extratropical coupling selectively enhances the variance of three principal modes of variability, explaining 13%, 11%, and 10% of the total variance of Pacific/North American, North Atlantic Oscillation, and Warm-Arctic Cold-Eurasian patterns, respectively. Atmosphere-ocean coupling reduces damping to lower-tropospheric available potential energy, which in turn increases kinetic energy by changing energy transfer within the mode. The extratropical ocean is overall passive (adjustable) to large-scale atmospheric variation, thus contributing to the prominence of these modes. The geographical dependence of available potential energy damping suggests the existence of mode-specific sweet spots where the influence of coupling operates efficiently, providing a clue to improving the model biases in variance and signal-to-noise ratio of these modes.

Large-scale, geographically fixed, recurrent patterns of atmospheric low-frequency variability are called teleconnection patterns^{1,2}. Their fluctuations are a manifestation of intensification, weakening, and meandering of the westerly jet streams in the extratropics and sometimes trigger extreme weather events^{3,4}. Therefore, it is crucial to clarify their generation and maintenance mechanisms for more skilful prediction and better future climate projection. The principal modes of low-frequency variability (i.e., the teleconnection patterns), including the North Atlantic Oscillation (NAO)^{1-3,5} and the Pacific/North American (PNA) pattern^{1,2}, owe their existence essentially to the dynamics inherent in the extratropical atmosphere⁶⁻¹¹, as can be simulated even under the condition of the climatological sea surface temperature (SST)^{12,13}. Nevertheless, SST variations in the tropics contribute to their prominence through Rossby wave propagation¹⁴ for triggering the variability^{15,16}.

Many theoretical, observational, and modelling studies have shown that the extratropical ocean can also influence the overlying atmospheric low-frequency variability, while its impact is modest compared to that from

the tropical ocean¹⁷⁻¹⁹. However, except for oceanic frontal regions where the ocean can actively influence the atmosphere¹⁹⁻²¹, basin-scale extratropical SSTs primarily respond passively to large-scale atmospheric fluctuations through anomalous surface turbulent heat fluxes, near-surface mixing and Ekman currents^{13,22-28}. The anomalous turbulent heat fluxes then act as thermal damping on the atmosphere toward their thermal equilibrium. Therefore, under an adjustable ocean, as in the actual coupled system, the damping of surface air temperature anomalies is expected to be weaker than that under a hypothetical non-adjustable ocean with an infinite heat capacity²⁹. This type of passive atmosphere-ocean coupling³⁰ based on the temperature adjustments, called reduced thermal damping³¹, is expected to yield an increase in low-frequency surface temperature variance^{18,31,32}.

In the late 1990s and early 2000s, some of the modelling studies using the general circulation models (GCMs) with relatively coarse horizontal resolutions¹⁹ (grid size greater than 100 km with no sharp ocean fronts) showed that the extratropical atmosphere-ocean coupling can enhance the overlying atmospheric low-frequency variability^{29,33-38}. However, results

¹Research Institute for Applied Mechanics, Kyushu University, Kasuga, Japan. ²Research Center for Advanced Science and Technology, The University of Tokyo, Tokyo, Japan. ³Faculty of Sustainable Design, University of Toyama, Toyama, Japan. ⁴Japan Agency for Marine-Earth Science and Technology, Yokohama, Japan. ✉e-mail: masato@riam.kyushu-u.ac.jp

were inconsistent across the studies^{34,39–41}, probably due to energetic internal variability in the extratropical atmosphere that is likely to mask the subtle signal^{18,41}. Besides, the impact of ocean dynamics was not taken into account in most studies. Therefore, the extent to which the passive atmosphere-ocean coupling enhances atmospheric low-frequency variability is still unclear. Furthermore, it also remains unclear how surface coupling enhances teleconnection patterns extending throughout the troposphere's depth. In this study, we thus revisit these issues using large-ensemble simulations with a moderate resolution state-of-the-art fully coupled climate model, focusing on the boreal winter (December through February) atmospheric year-to-year variability in the extratropical Northern Hemisphere.

We performed two sets of large-ensemble experiments (see “Methods”). One is a coupled experiment with the atmosphere-ocean-land coupled GCM (CGCM) (referred to as C-run), and the other is an uncoupled experiment with the atmospheric component (AGCM) of the same CGCM (A-run). The C-run is based on Coupled Model Intercomparison Project Phase 6 (CMIP6) historical and scenario simulations from 1979 to 2020 with 50 ensemble members. For each member of the A-run, the AGCM is forced by monthly mean SST and sea ice boundary conditions obtained

from each of the 50 members of the C-run. Hence, the monthly mean SST and sea ice are identical between the two corresponding experiments. However, the A-run does not include the two-way air-sea interaction at each model time step. Therefore, any difference in statistics between the two experiments can be interpreted as a coupling effect.

Results

Difference in Northern Hemisphere wintertime atmospheric variability with and without air-sea coupling

Figure 1 compares interannual variances of DJF-mean 500-hPa geopotential height (Z500) and sea level pressure (SLP) anomalies in the Northern Hemisphere between the C- and A-runs. For both variables, the C-run shows significantly higher values around the variance local maxima, especially in the North Pacific, subpolar North Atlantic, and northern Eurasia around the Barents-Kara Seas (Fig. 1a–d). The fractional increase exceeds 10% in these regions from the surface into the upper troposphere (Supplementary Fig. 1). This increase indicates that the presence (absence) of atmosphere-ocean coupling significantly enhances (suppresses) tropospheric variability in the extratropics. The increased Z500 variance in the North Atlantic is consistent with the results of Bladé (1997)³⁵, who

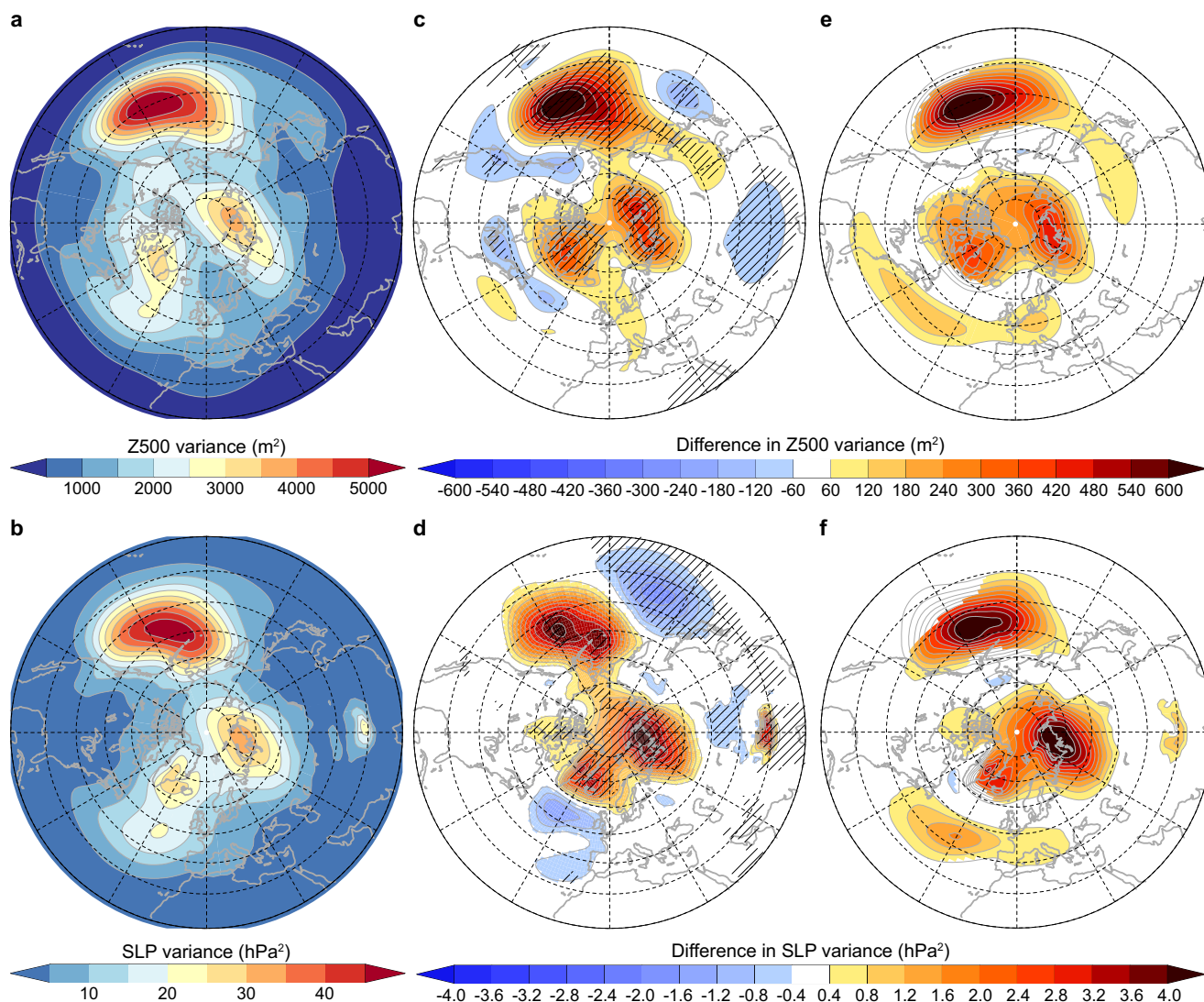


Fig. 1 | Difference in winter atmospheric variability with and without coupling. Variance for DJF-mean anomalies of Z500 (a, unit is m^2) and SLP (b, hPa^2) in the C-run. Difference in Z500 (c) and SLP (d) variance between the C- and A-runs (C-run minus A-run). The hatching indicates the statistical confidence for the difference

exceeding 95% level, based on two-sided *F*-test. e, f, Same as (c, d), but reconstructed from the three leading EOT modes of Z500 variability (coloured only where the statistical confidence exceeds 95% level based on two-sided *F*-test).

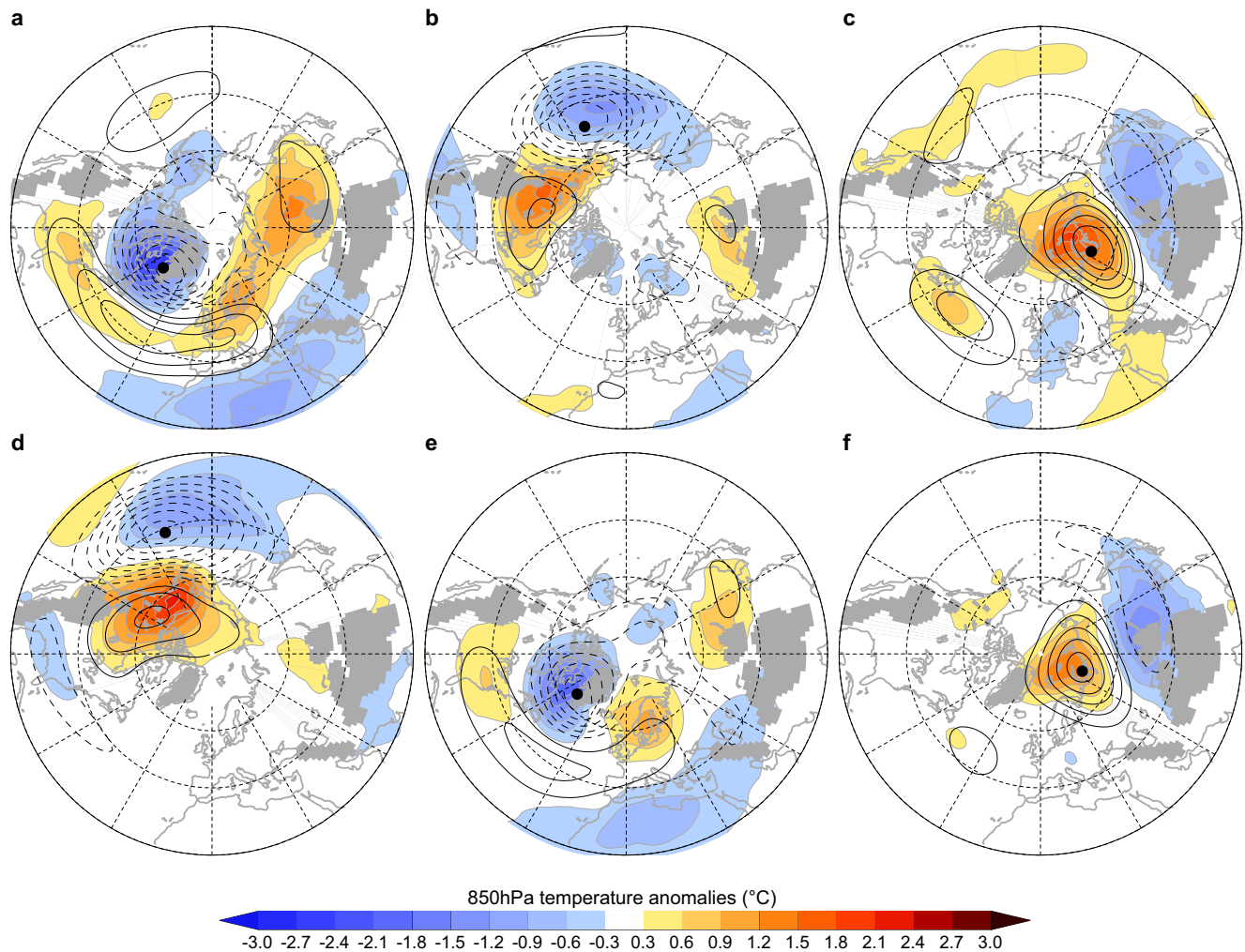


Fig. 2 | The leading three patterns of NH winter atmospheric variability. DJF-mean Z500 (contours at 10 m intervals, dashed if negative) and T850 (shading, °C) anomalies from JRA-55, associated with the EOT1 (a), EOT2 (b), and EOT3 (c), respectively. **d-f** Same as (a-c), but for anomalies from the C-run. Displayed as a

regression of local Z500 and T850 anomalies onto the standardised expansion coefficient of EOT. Black circles indicate EOT base points. The analysis domain is the Northern Hemisphere poleward of 20°N.

contrasted simulation by an AGCM coupled with an ocean mixed-layer model to an uncoupled AGCM simulation driven by climatological SST (i.e., there is no El Niño-Southern Oscillation (ENSO)-related signal). Though weaker in magnitude, there are also significant decreases in variance in some other regions, particularly in the western North Pacific, central Eurasia, and part of the midlatitude North Atlantic.

To understand what differences in atmospheric circulation patterns are responsible for the variance changes, we applied empirical orthogonal teleconnection (EOT) analysis^{42,43} to the DJF-mean Z500 anomalies in the simulations and the Japanese 55-year Reanalysis (JRA-55) data (see “Methods”). Unlike empirical orthogonal function analysis, EOT analysis is not affected by spatial orthogonality constraints and thus is likely to extract physically meaningful patterns, even in higher-order modes⁴³. Figure 2 shows the three leading EOT modes of the Northern Hemisphere wintertime Z500 variability. In JRA-55, the first mode, EOT1, represents the NAO^{1-3,5}, also known as the Northern Hemisphere annular mode⁴⁴. The second mode, EOT2, corresponds to the PNA pattern^{1,2}. The third mode, EOT3, depicts variability with its primary centre of action around the Ural at the surface (Supplementary Fig. 2). This pattern has been attracting attention recently and is referred to by different names in the literature, for example, the Russian (RU) pattern⁴⁵, the Warm-Arctic Cold-Eurasian/East Asian (WACE) pattern^{45,46}, and also may correspond to the Eurasian Type1 (EU1) pattern². The EOT

circulation anomaly patterns significantly impact surface and lower-tropospheric temperature variability in the surrounding regions^{3-5,43,45} (Fig. 2 and Supplementary Fig. 2). Both coupled and uncoupled simulations capture well the spatial structure of these principal modes (Fig. 2 and Supplementary Fig. 3) but are biased in reproducing their magnitude, and the order of the first and second modes is flipped. Namely, the PNA variability is overestimated, while NAO and WACE are weak in the MIROC6 model compared to JRA-55. The PNA and NAO magnitude biases are typical in recent climate models^{47,48}.

Comparison of the variance explained by each EOT mode between the C- and A-runs reveals that the presence of air-sea coupling significantly enhances the Z500 variance of the three leading modes (Fig. 3) and the 8th mode, which corresponds to the North Pacific Oscillation^{1,49,50} (NPO, Supplementary Fig. 4b). No significant differences are found in other higher modes, including the 4th mode, which corresponds to the western Pacific (WP) pattern^{1,49,51,52} (Supplementary Fig. 4a). The significant variance increase is due to the increased magnitude of anomalies of those EOT modes rather than to slight changes in their spatial structure. In fact, even if the EOT is applied separately for the C- and A-runs, the coupling does not change the order of modes, and their spatial structure is virtually indistinguishable between the two runs (Supplementary Fig. 5). In summary, the atmosphere-ocean coupling selectively affects the intensity of the three principal modes (and the 8th mode) while retaining their spatial structure as

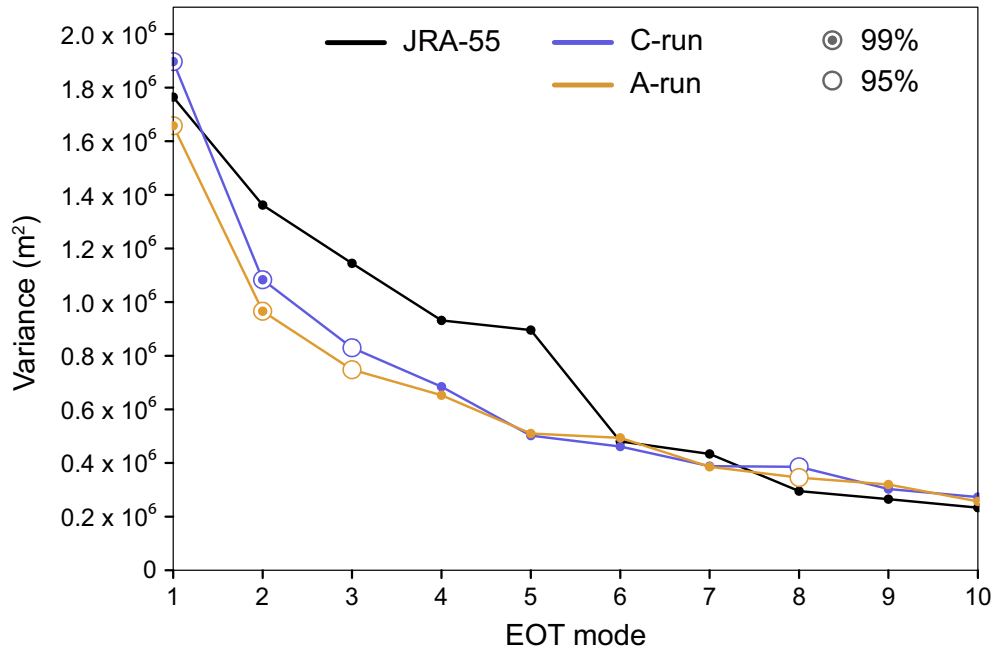


Fig. 3 | Comparison of the variance explained by each EOT mode between coupled and uncoupled simulations. Variance explained by each EOT mode of DJF-mean Z500 anomalies in the C-run (purple line), A-run (orange line), and JRA-55 reanalysis (black line) derived from Eq. (1). Double and open circles indicate that the

variance is significantly different between the C- and A-runs at 99% and 95% levels, respectively, based on two-sided *F*-test. Before EOT analysis, Z500 anomalies in JRA-55 reanalysis had been interpolated to the spectral model grid.

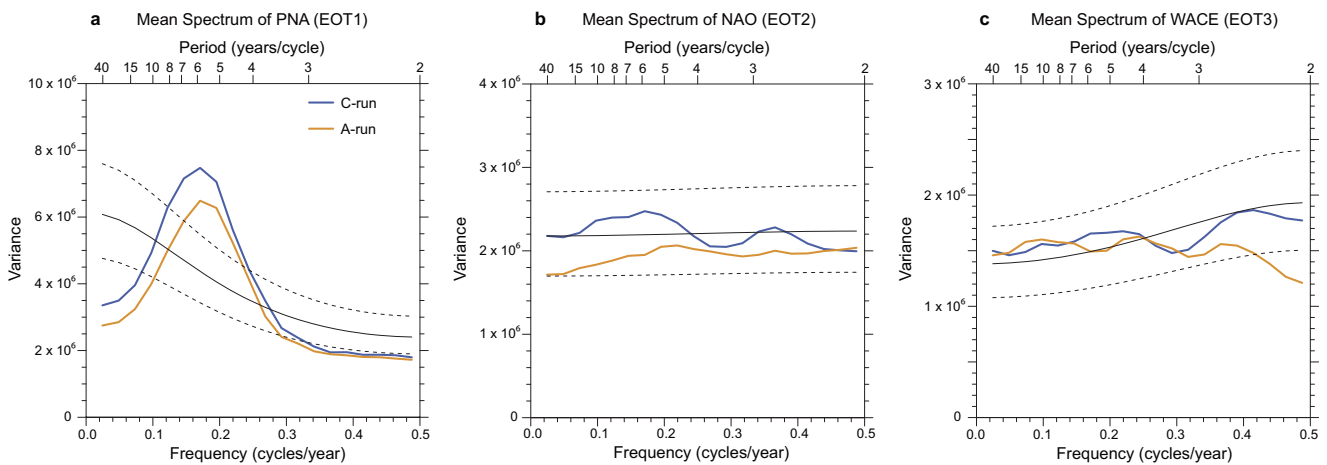


Fig. 4 | Comparison of the power spectrum of the three leading EOT modes between coupled and uncoupled simulation. Ensemble-averaged power spectrum of the EOT1 (a), EOT2 (b), and EOT3 (c) for the C-run (purple) and A-run (orange),

shown as a function of frequency (“Methods”). Black solid and dotted lines indicate the theoretical Markov spectrum and its lower (5%) and upper (95%) confidence curves for the C-run.

in the uncoupled run. We hereafter refer to this phenomenon as selective enhancement.

Consistent with the selective enhancement, the three leading modes in the C-run show more pronounced anomalies in SLP, surface air temperature (SAT), and 850hPa temperature (T850) than in the A-run (Fig. 2 and Supplementary Figs. 2, 3). Hence, we have reconstructed Z500 and SLP variance for each simulation only from the three leading modes. The difference between the C- and A-runs of the reconstructed Z500 variance explains the increase in total variance due to coupling well (Fig. 1c, e). The same applies to the associated SLP variance (Fig. 1d, f). The prominent variance difference at the North Pacific, North Atlantic, and northern Eurasia in Fig. 1c, d can be explained by the enhancement of PNA, NAO, and both WACE and NAO, respectively (Supplementary Fig. 6). Therefore, the increase in winter atmospheric low-frequency variance due to the

atmosphere-ocean coupling (Fig. 1a–d) is primarily attributed to the selective enhancement of the three leading modes of variability.

To clarify which timescales of variability are responsible for the variance differences, we have applied spectral analysis to the time series of each EOT mode (“Methods”). While NAO and WACE show no significant spectral peaks (Fig. 4b, c), the PNA pattern has a significant peak of (4–8 years)^{−1} corresponding to the ENSO frequency (Fig. 4a), consistent with the observational estimates⁵³. This suggests that part of the PNA pattern is forced by ENSO^{8,14,34,39–41}. A comparison of the spectra between the C- and A-runs reveals that the enhancement of variance due to coupling is mainly accomplished by the low-frequency bands below about (2.8 years)^{−1} for PNA and (2.4 years)^{−1} for NAO (Fig. 4a, b). Therefore, the enhancement of PNA and NAO arises from enhancement in interannual to decadal variability. In contrast, the variance increase for WACE is achieved mainly in

interannual variability with high-frequency bands above $(3.2 \text{ years})^{-1}$ (Fig. 4c).

We emphasise that the selective enhancement can only be robustly identified using large samples. Indeed, Fig. 5 shows that the robust variance difference for PNA, NAO, and WACE cannot be detected with less than 25, 15, and 30 ensemble members, respectively (note that each member contains 41 winters). This means that the coupling effect is generally smaller than the spread of interannual variability and thus easily obscured (i.e., the low signal-to-noise ratio¹⁸). Nevertheless, it is not necessarily negligible, as it explains approximately 13%, 11%, and 10% of the total variance in the respective modes of PNA, NAO, and WACE (Figs. 3, 5).

To understand the mechanisms by which coupling alters the variance of the principal modes, we first examine the remote influence from the tropics. Since interannual variability of the winter-mean PNA pattern has a large projection onto ENSO-forced atmospheric variability^{8,14,34,39–41}, we begin by focusing on the difference in the PNA pattern between the C- and A-runs. Note that El Niño and La Niña events occur at the same time in both the C- and A-runs. Supplementary Table 1 shows the correlation coefficients between the ENSO and PNA indices (i.e., $EC1_C$ and $EC1_A$; “Methods”). The PNA in this model shows the highest correlation with the Niño 4 index at 0.66 and 0.64 in the C- and A-runs, respectively, indicating that ENSO explains at most 43% and 40% of the PNA variance in those simulations. Therefore, the coupling effect on PNA variation described above (13% of the total PNA variance) cannot be explained by the difference in ENSO-related forcing in the tropics between the two runs. Similarly, it cannot be explained by the differences in the influence from other tropical regions during DJF (Supplementary Table 2), preceding SON (Supplementary Table 3), and JJA (Supplementary Table 4) seasons. These results suggest that extratropical atmosphere-ocean coupling can be essential for the variance increase in the PNA. This is also true for the NAO and WACE (Supplementary Tables 1–4).

Difference in PNA with and without coupling

Next, we investigate the influence of extratropical atmosphere-ocean coupling. It is clear from Fig. 6a, b that the PNA-associated SLP and T850 anomalies are nearly in quadrature, indicating a baroclinic structure of the PNA pattern in the lower troposphere. The positive phase of the PNA (with the deeper Aleutian Low) brings colder and drier airmass from the subpolar East Asian continent into the midlatitude central Pacific (contours in Fig. 6b). In the C-run, anomalous surface westerlies centred around 35°N (Fig. 6b) induces an increase in upward turbulent heat flux (THF; latent and sensible heat fluxes) by intensifying the climatological westerly wind speed and air-sea differences in temperature and humidity (Fig. 6a)^{23,24,34,40,41}. This upward THF anomaly warms the near-surface atmosphere and simultaneously cools the ocean surface to reduce the air-sea thermal difference, leading to the thermal damping of the cool and dry continental airmass. The positive PNA also brings warmer and wetter airmass from the subtropical eastern Pacific to the west coast of the North American Continent (Fig. 6b). The associated downward THF anomaly also acts as thermal damping of the warmer and moister airmass.

Compared with the C-run, the THF anomalies in the uncoupled A-run are stronger in the central Pacific around 35°N (Fig. 6d), despite the weaker atmospheric circulation anomalies. It indicates stronger thermal damping in the A-run, where only the atmosphere is allowed to adjust toward an air-sea thermal equilibrium. As a result, the negative T850 anomalies in the midlatitude central Pacific are weaker than in the C-run (Fig. 6e).

The above explanation also holds for the negative phase of the PNA with the reversed sign. Therefore, the differences in thermal damping between the two runs are depicted by the differences in THF variance (Fig. 6f), which shows that the atmosphere-ocean coupling reduces the thermal damping and increases the variance of thermal anomalies in a broad region of the mid-latitude Pacific. This reduced thermal damping mechanism³¹, originally derived from a simple one-dimensional energy balance equation, seems to be a key mechanism for explaining the increased PNA variance due to the extratropical atmosphere-ocean coupling

(contours in Fig. 6f). This is consistent with our spectral analysis, which shows the coupling enhancement on interannual to decadal timescales (Fig. 4a). However, the reduced thermal damping mechanism explains the increase in surface air temperature variability due to coupling, but not the intensification of any specific dynamical (i.e., atmospheric circulation) anomalies. This point will be investigated in the next section.

In the A-run, SST is not allowed to respond to atmospheric fluctuations. However, the SST significantly correlates with the PNA variation, showing a horseshoe-shaped anomaly pattern (Fig. 6e) as in the C-run. This is because part of the PNA variance arises from the common ENSO forcing between the C- and A-runs. When ENSO forces a PNA-like anomaly and, thereby, mid-latitude SST anomalies in the C-run, the resultant SST anomaly is given in the corresponding A-run. Therefore, if the PNA is simultaneously excited in the A-run as in the C-run, the former would correlate with the mid-latitude SST anomalies, even if there is no coupling. Thus, the extratropical coupling effect is partly included in the A-run due to our experimental design, and the total extratropical coupling effect should therefore be stronger than suggested from the comparison of the C- and A-runs.

Oceanic Ekman heat transport is another important factor that can affect the air-sea temperature difference, especially in oceanic frontal zones^{28,41}. In the C-run, the surface wind stress anomalies associated with the positive PNA lead to anomalous equatorward (poleward) Ekman transport to the south (north) of 40°N in the central (eastern North) Pacific, greatly contributing to the formation of cool (warm) SST anomalies there (Fig. 6c). This anomalous Ekman heat transport can impact the SST anomalies comparably to or even more than the THF anomalies^{28,41}. Therefore, ocean dynamics also play an essential role in reducing the air-sea temperature difference (i.e., reducing thermal damping). However, due to the experimental design, the SST influenced by Ekman heat transport is prescribed to the AGCM. As a result, part of the impact of Ekman heat transport has also been implicitly included in the A-run, and therefore the difference between the C- and A-run is likely to underrepresent the actual coupling effect. Specifically, PNA would be more strongly damped in an uncoupled simulation where, for example, climatological SST is prescribed in the mid-latitudes.

Difference in NAO with and without coupling

Next, we focus on the difference in the NAO between the C- and A-runs (Fig. 7). The analysis suggests that, as in the PNA, the reduced thermal damping mechanism is fundamentally important, but model biases make it challenging to detect its influence. As the variance difference indicates, the NAO-associated SLP and T850 anomalies are more prominent in magnitude in the C-run than in the A-run (Fig. 7a, b, d, e). The positive phase of the NAO (with the stronger Iceland Low and Azores High) brings colder and drier airmass from Canada into the North Atlantic subpolar gyre region including the Labrador Sea (contours in Fig. 7b, e) by stronger westerlies. In both runs, the surface westerly anomalies (vectors in Fig. 7b, e), centred around 55°N, increase upward THF in this region to reduce the air-sea temperature and humidity differences (Fig. 7a, d). This THF anomaly thermally damps the incoming colder and drier airmass and, only in the C-run, simultaneously cools the ocean surface^{22–27}. Thus, the SST anomalies in the subpolar gyre region become overall negative in the C-run (Fig. 7b). In contrast, they show a weaker correlation with the NAO in the A-run (Fig. 7e). As a result, in the subpolar gyre region, thermal damping to the atmosphere is considered to be weaker in the C-run than in the A-run. However, contrary to this inference, in a part of the subpolar gyre region around [50°W, 55°N], the THF anomaly is stronger in the C-run (Fig. 7a, d, f). This is caused by the model biases, as will be discussed next.

In the C-run, positive SST anomalies, not found in the observation (Supplementary Fig. 7a), are simulated in the region around [50°W, 55°N] (Fig. 7b). This region corresponds to where the mixed layer depth anomalies reach their maximum (Supplementary Fig. 7b). This model bias is attributable to the bias in the vertical profile of climatological ocean temperature (Supplementary Fig. 7a). In the model, as the NAO deepens the oceanic

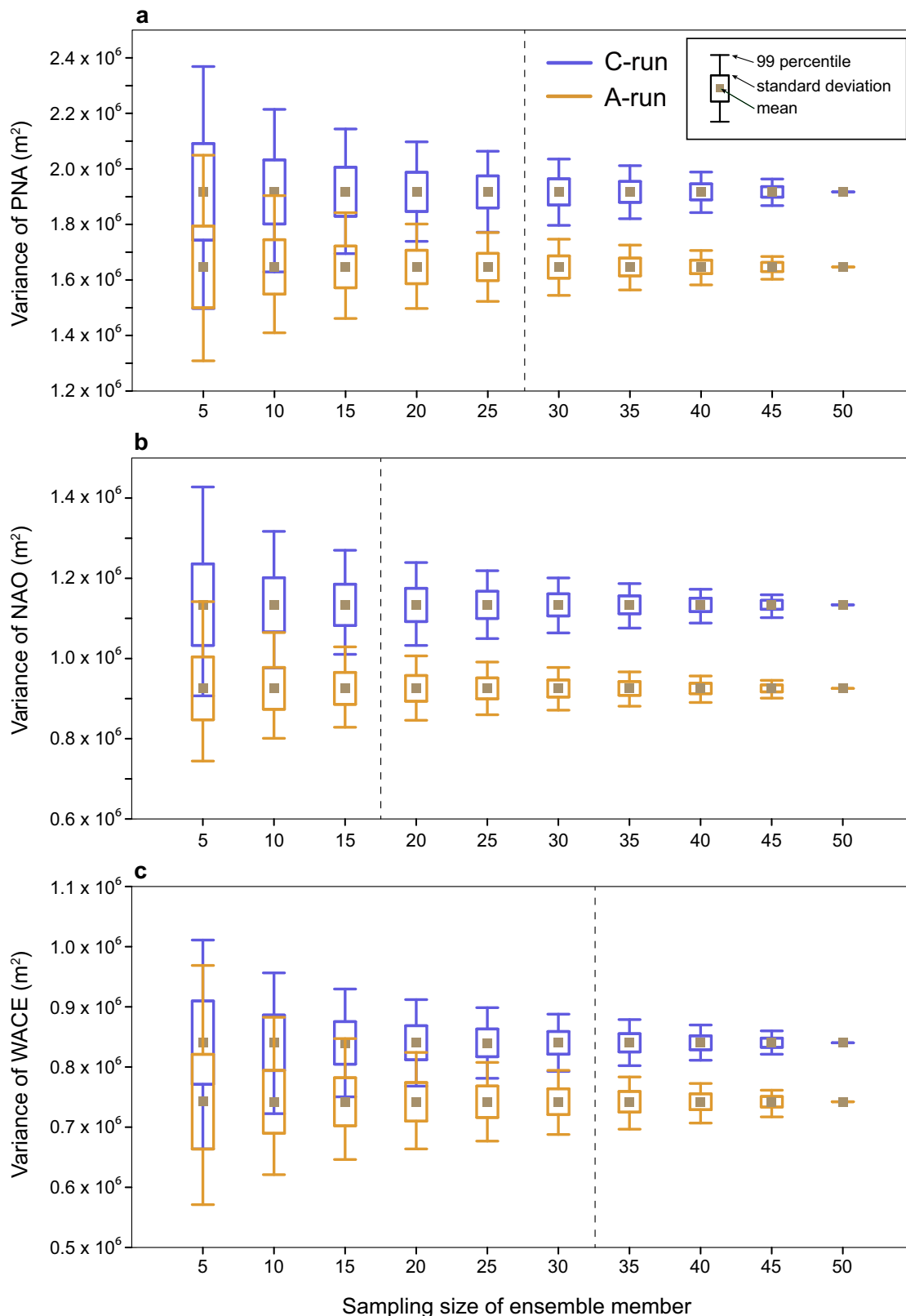


Fig. 5 | Robustness and dependence of coupling effect detection on ensemble size.

Box-and-whisker plots of the ensemble-mean variances explained by respective EOT modes for the C-run (purple) and A-run (orange), shown as a function of ensemble size. EOT1 (a), EOT2 (b), and EOT3 (c). Boxes and whiskers indicate

ranges of one standard deviation and the 99th percentile, respectively, and are estimated based on bootstrap random sampling (100,000 times). Vertical dashed lines indicate the minimum number of ensemble members required for robust signal detection at the 99% confidence level.

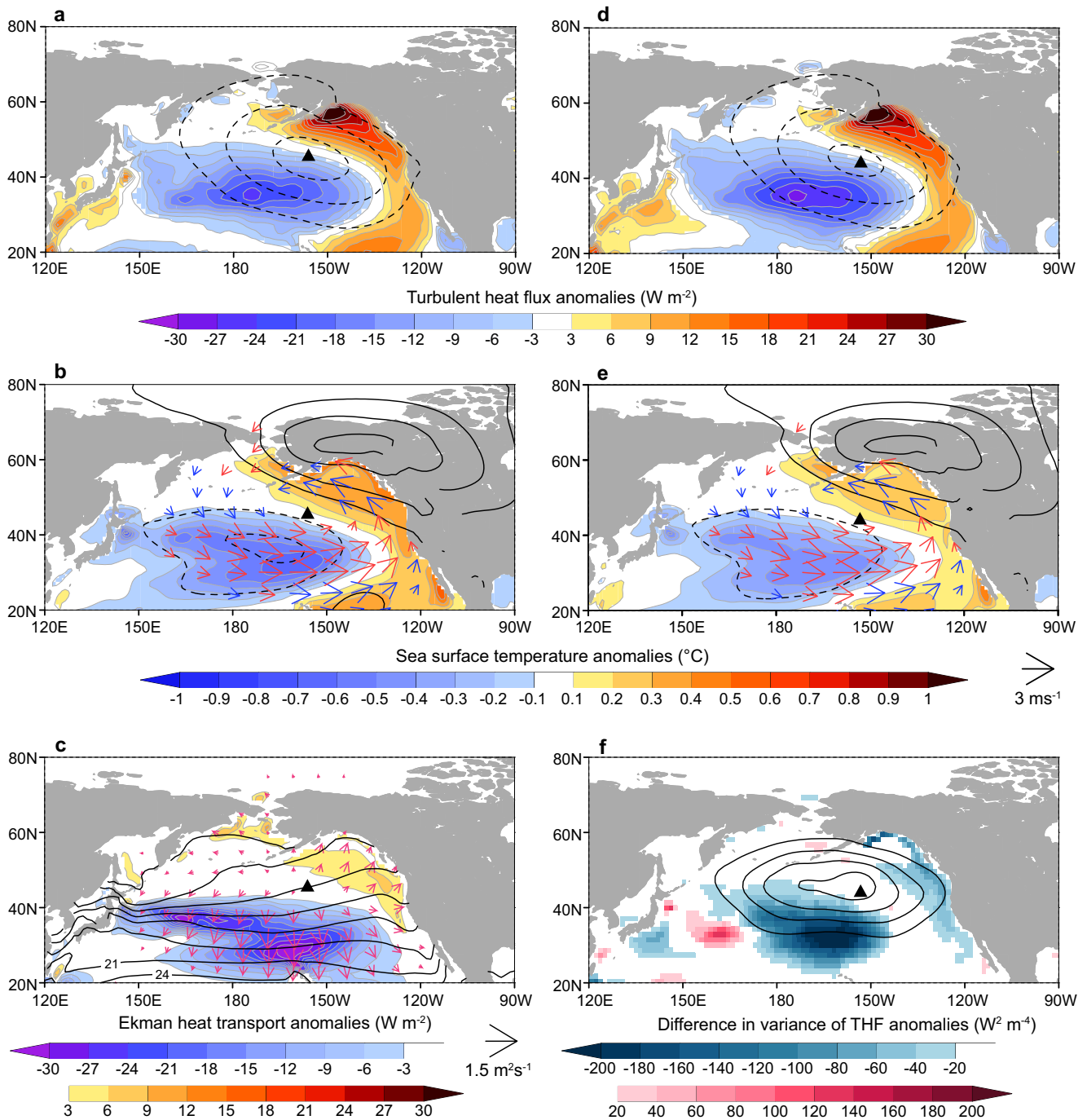


Fig. 6 | Atmosphere-ocean interaction for PNA in the coupled and uncoupled simulation and its difference. Anomalies for DJF-mean SLP (a; contours at 2hPa intervals), THF (a; shading, downward positive, $W m^{-2}$), T850 (b; contours at $0.5^{\circ}C$ intervals), SST (b; shading, $^{\circ}C$), 10 m wind (b; vectors, ms^{-1}), oceanic Ekman transport (c; vectors, m^2s^{-1}) and associated heat transport expressed as equivalent surface energy flux (c; shading, SST warming direction is positive, $W m^{-2}$) from the C-run, regressed onto the $EC1_C$. Contours are dashed if negative. Coloured only where the statistical confidence exceeds 99% level based on two-sided t test. The 10 m

wind anomalies in (b) are shown in red if they increase scalar wind speed and in blue if they reduce it. Contoured in (c) are SST climatology ($3^{\circ}C$ intervals). d, e, Same as (a, b), but for anomalies from the A-run, regressed onto the $EC1_A$. f Difference in the variance of SLP (contours at $1hPa^2$ intervals, dashed if negative) and of THF anomalies (shading; coloured only where the statistical confidence exceeds 95% level based on two-sided F -test) associated with the EOT1 (C-run minus A-run). The black triangle indicates the centre of SLP anomalies in the North Pacific.

mixed layer, warmer subsurface water is continuously transported to the surface (Supplementary Fig. 7b). Resultant unrealistic positive SST anomalies in the C-run appear to cause excessive heat release into the atmosphere (Fig. 7a, d), resulting in stronger thermal damping than in the A-run in this region (Fig. 7f). Nevertheless, we will find that the net thermal damping in this region is greater in the A-run than in the C-run at 850hPa,

as discussed in the next section. This model bias may contribute to too weak variability of simulated NAO (Fig. 3).

In the C-run, the surface wind stress anomalies associated with the positive NAO lead to anomalous equatorward Ekman transport to the north of $40^{\circ}N$, contributing to the formation of cool SST anomalies around the oceanic frontal zone where meridional SST gradients are climatologically

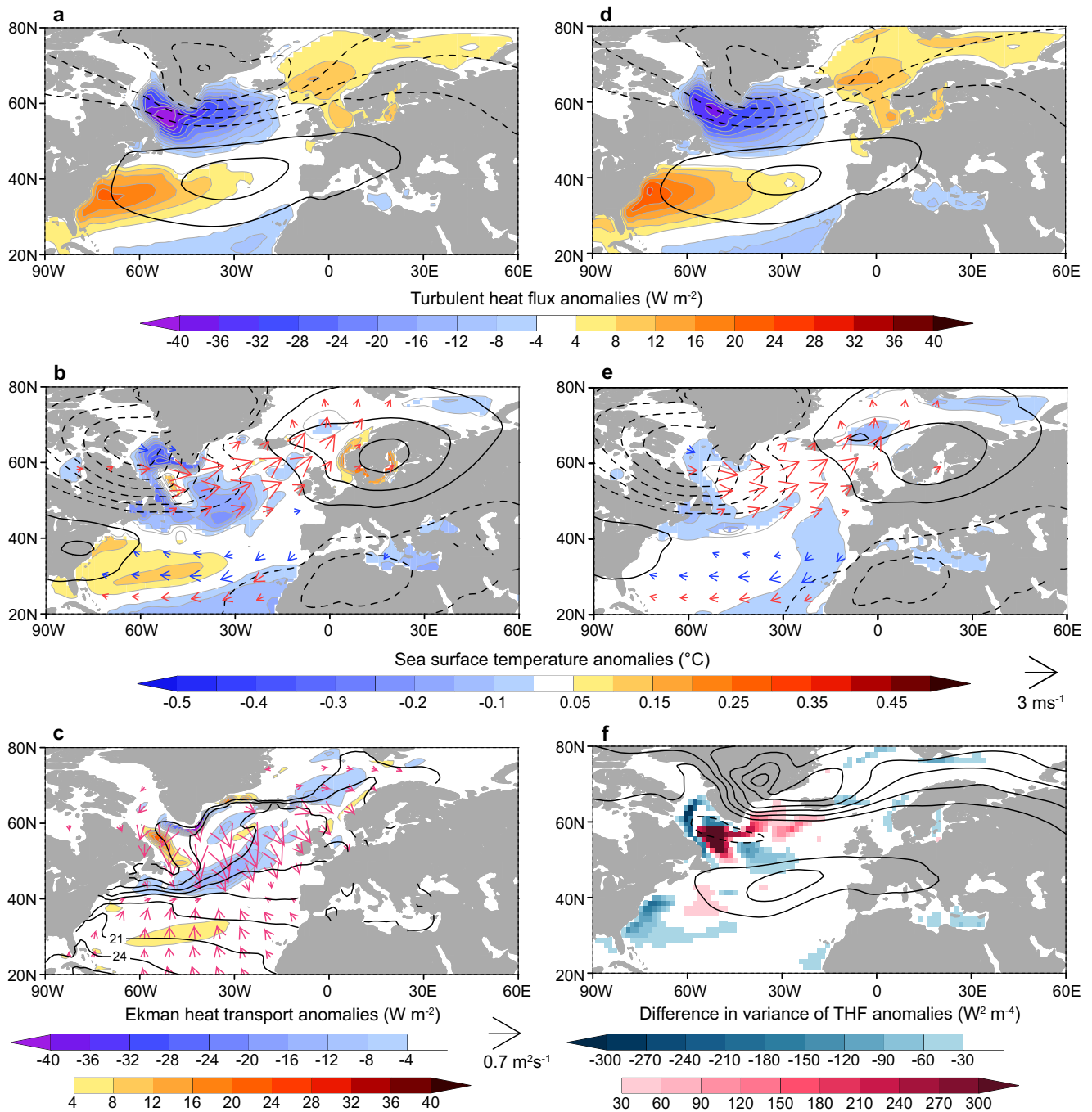


Fig. 7 | Atmosphere-ocean interaction for NAO in the coupled and uncoupled simulation and its difference. Same as Fig. 6 but for anomalies regressed onto the respective EC2. Contours intervals are 1hPa in (a) and (d), 0.3°C in (b, e), 3°C in (c), 0.5hPa² in (f).

pronounced (Fig. 7c)^{25,26,54}. This effect is comparable to the THF (Fig. 7a) and thus not negligible²⁵. The resultant cool SST anomalies weaken the air-sea temperature difference, thus contributing to the reduction of thermal damping to the atmospheric anomalies in the southern part of the subpolar gyre region. Ocean dynamics therefore also play an important role in shaping the difference in thermal damping between the two runs.

Energetics of PNA and NAO with and without coupling

To understand how the atmosphere-ocean coupling dynamically enhances the circulation variability through the change in thermal damping, we investigate the difference in the energetics of the PNA and NAO between the C- and A-runs (“Methods”). The kinetic energy (KE) accounts for a larger proportion of the total energy of those modes than the available potential

energy (APE) (Fig. 8a, c). However, the opposite is true for the lower and middle troposphere, reflecting baroclinic structures of the PNA and NAO, especially in the lower troposphere^{55–57}. The amount of total energy indicates that both the PNA and NAO are more energetic in the C-run than in the A-run (Fig. 8a, c), consistent with the variance differences (Fig. 3).

We compare the energy conversion efficiencies to assess the relative importance of various processes in generating this energy difference (Fig. 8b, d). Note that the energy conversion efficiency, evaluated by dividing the energy conversion term by the total energy after spatial integration^{55,58}, is independent of the magnitudes of the patterns (“Methods”). The thermal damping through heat exchange with the ocean, discussed in the preceding sections, is included in the diabatic forcing term (CQ) in the APE budget equation (Eq. (3)). Hence, the

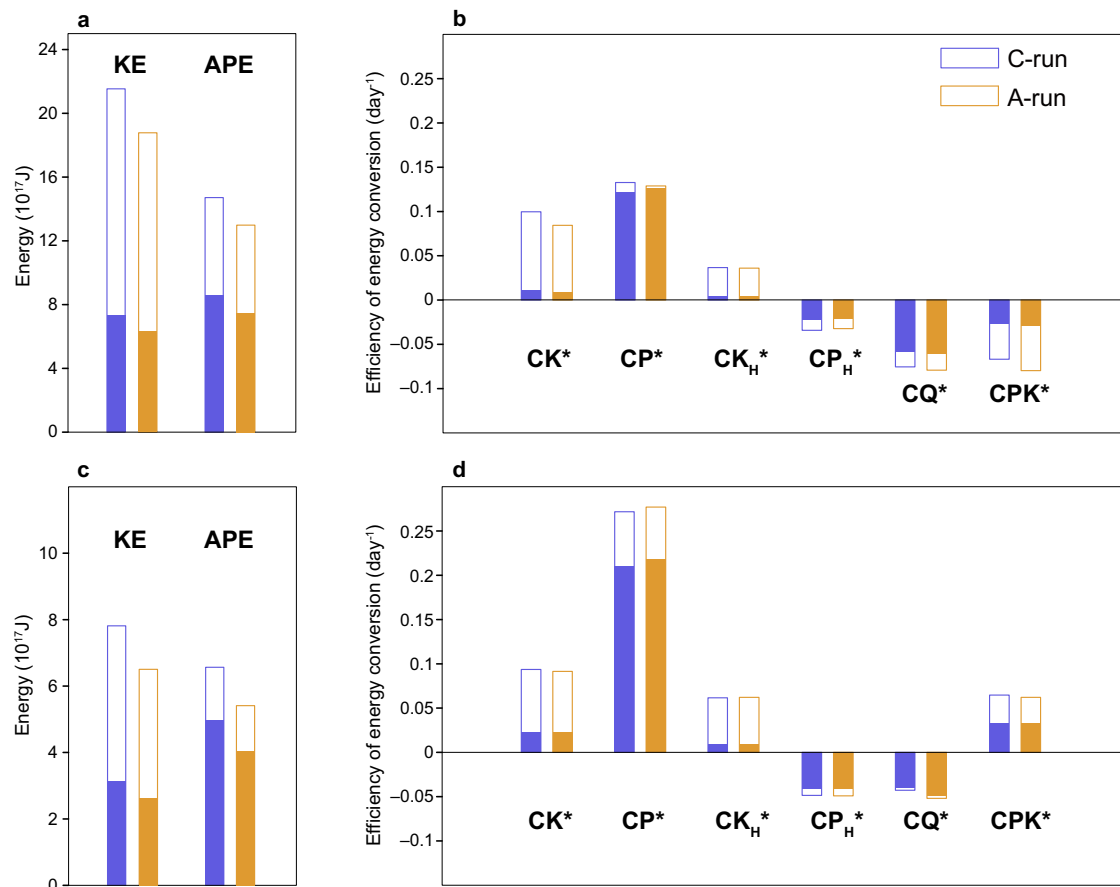


Fig. 8 | Difference in energy conversion efficiency between coupled and uncoupled simulations. KE and APE (a, c), and efficiency of energy conversion terms (b, d; day⁻¹) associated with the PNA in the C-run (purple) and A-run (orange). All variables are integrated over the extratropical Northern Hemisphere (0°–360°E, 20°–90°N) and vertically from the surface to 200hPa. The vertical integrals from the

surface to 500hPa are indicated with filled boxes and the remaining are shown in open boxes. CK and CP denote barotropic and baroclinic energy conversions from the climatological-mean fields, CK_{HF} and CP_{HF} barotropic and baroclinic feedbacks, respectively, from transient eddies, CQ diabatic APE generation, and CPK conversion from APE to KE. c, d, Same as (a, b), but for NAO.

coupling directly affects the efficiency of CQ (referred to as CQ*) in the lower troposphere. Consequently, for both the PNA and NAO, net CQ* is negative in both runs (i.e., damping on APE), and its magnitude is smaller in the C-run in the lower troposphere (coloured bars in Fig. 8b, d).

We then examine the spatial pattern of CQ at 850hPa. The PNA in the C-run shows prominent APE loss in the mid-latitude central Pacific (around 35°N) and near the Gulf of Alaska, with notable but narrow APE generation around [60°N, 150°W] (Fig. 9a). For the positive PNA, for example, the negative CQ in the central Pacific indicates that the cold lower-tropospheric anomalies are weakened by anomalous diabatic heating (see Fig. 6a, b). Decomposing the CQ into contributions from the individual physical processes reveals that the vertical diffusion (by turbulence), the cumulus and shallow convection are the main contributors to the heating anomalies in this region (Supplementary Fig. 8), implying the influence of surface THF. The negative CQ near the Gulf of Alaska is mainly caused by shallow convection and cloud physics heating, while the positive CQ around [60°N, 150°W] is mainly caused by vertical diffusion and large-scale condensation heating (Supplementary Fig. 8). The CQ difference between the two runs shows that the damping on APE is weaker in the C-run over the central Pacific (Fig. 9b). This is mainly due to the difference in the vertical diffusion heating (Supplementary Fig. 8), illustrating the key role of surface sensible heat flux difference due to coupling, whose influence extends into the free troposphere.

For the NAO, 850hPa CQ in the C-run is negative around the Labrador Sea, mostly due to the vertical diffusion heating anomalies (Fig. 9c and

Supplementary Fig. 9). This indicates that the damping effect on APE by the ocean reaches the lower troposphere. The CQ differences between the C- and A-runs show that the net damping is weaker in the C-run in this region (Fig. 9d), mostly due to the difference in vertical diffusion heating. There is a narrow region around [50°W, 55°N] where the damping is stronger in the C-run. This is the region where the excessive THF anomalies are observed due to the model biases (see the previous section and Fig. 7). Still, this contribution is rather minor, and the net effect of atmosphere-ocean coupling reduces the APE damping in the lower troposphere also for the NAO. It is worth noting that the lower tropospheric APE associated with the NAO maximises in the vicinity of the strongest thermal damping (Fig. 9c and Supplementary Fig. 10b). Similarly, local maxima of the lower-tropospheric APE associated with the PNA are also located where the thermal damping is relatively strong (Fig. 9a and Supplementary Fig. 10a), suggesting the potential importance of their baroclinic structure for effectively reaching the influence of the sea surface heat exchange into the free troposphere.

As shown in Fig. 8b, d, in both runs, the PNA and NAO are mainly maintained by barotropic energy conversion (CK*) in the upper troposphere^{6,8,11} and baroclinic energy conversion (CP*) in the middle and lower troposphere^{55,57}. Feedback forcing from modulated storm track activity, especially CK_{HF}*, also contributes to the maintenance of PNA^{7,9,10,57} and NAO^{7,9,55–57}, although the net feedback (CK_{HF}* + CP_{HF}*) is rather small. The modified APE damping induces changes in overall energy transfer via slight structural changes in the circulation anomalies. For the PNA, for example, the sum of conversion efficiencies for the net APE generation (CP* + CP_{HF}* + CQ*) is higher in the C-run, which is offset by

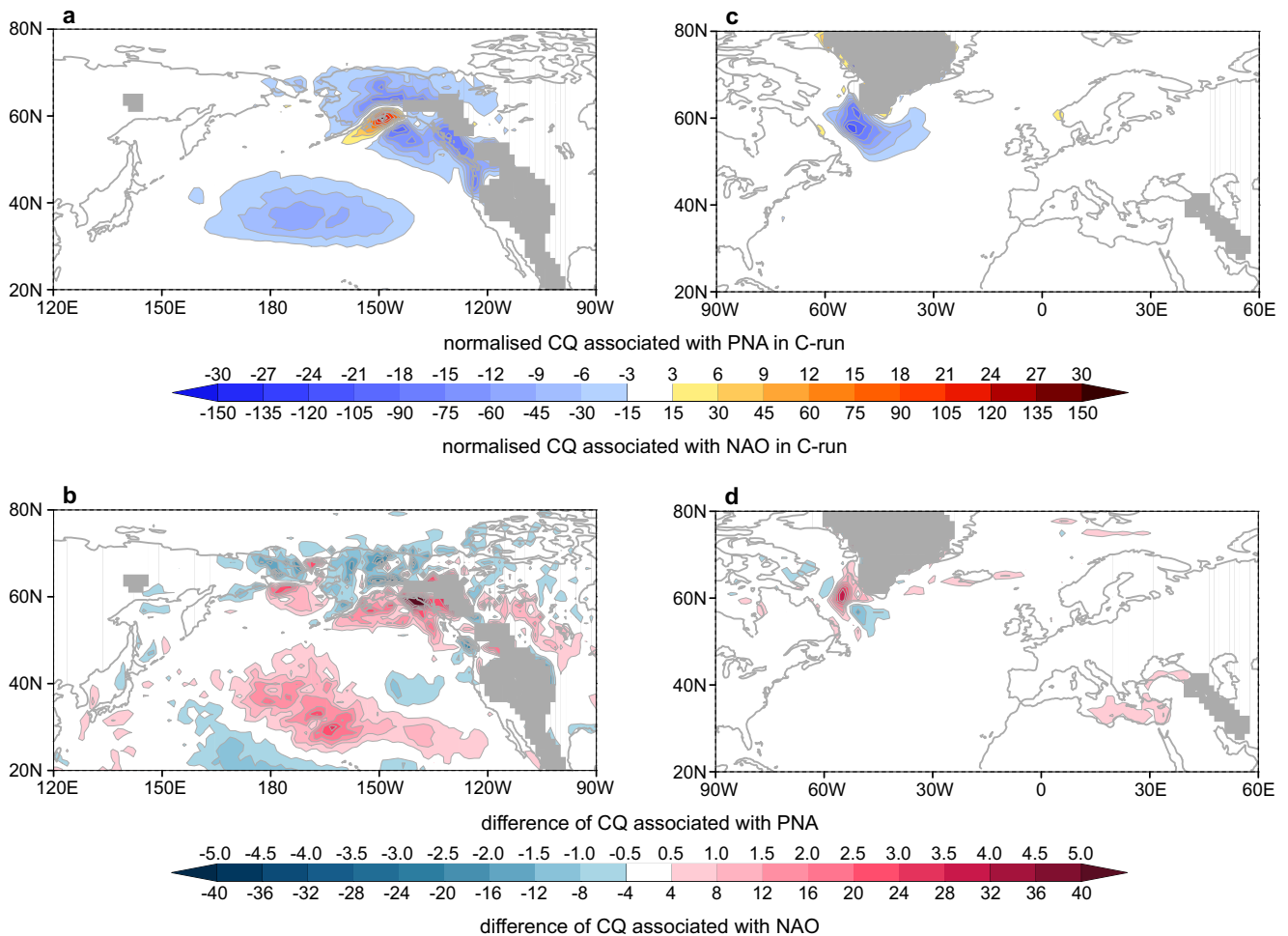


Fig. 9 | Comparison of diabatic APE generation CQ between coupled and uncoupled simulations. Normalised CQ at 850hPa associated with the PNA for the C-run (a; $10^{-19} \text{kg}^{-1} \text{day}^{-1}$) and its difference between the C- and A-runs (b; $10^{-19} \text{kg}^{-1} \text{day}^{-1}$). c, d, Same as (a, b), but for NAO. Note that the CQ differences

represent its change due to the coupling, independent of the magnitude difference in PNA or NAO because CQ is normalised by the total energy of PNA or NAO (sum of KE and APE in Fig. 8a, c) in each run.

a lower conversion efficiency from KE to APE (negative CPK*). This change in CPK* means smaller damping to KE, which in turn contributes to greater KE in the C-run. The greater CK* in the C-run also contributes to the greater KE; there may be a mechanism by which the change in energy balance triggered by the modified CQ* enhances CK*. For the NAO, the sum of conversion efficiencies for net APE generation ($\text{CP}^* + \text{CP}_{\text{HF}}^* + \text{CQ}^*$) is also higher in the C-run, which is offset by a higher conversion efficiency from APE to KE (positive CPK*). This change in CPK* implies that the net KE gain is larger in the C-run, contributing to the greater KE. In summary, the extratropical atmosphere-ocean coupling leads to a change in the dynamical balance governing the energy transfer within the patterns through reduced APE damping, resulting in an increase in KE and APE.

Figure 10 shows scatter plots of APE and KE obtained for individual ensemble members. Due to the stochastic nature of the modes, there is a large spread of energy among the members, but APE and KE are highly correlated for each of the three leading modes. It implies that the changes in APE can lead to changes in KE and vice versa and that the proportions of KE and APE in the total energy are roughly predetermined by the dynamics governing the mode and vary among the modes; the proportion of KE is highest in PNA, followed by NAO and then WACE. Meanwhile, as shown in the preceding section, the coupling leads to the change in energy transfer within the mode, resulting in systematic changes in the energy, as represented by the difference in the ensemble average of KE and APE between the

two runs (ΔKE and ΔAPE) (Fig. 10). Then, the direction of the systematic change does not appear to deviate significantly from the linear regression line that would be determined by the dynamics governing the mode. This is consistent with the fact that the coupling effect is not strong enough to alter the spatial structure of the mode significantly. All EOT modes selectively enhanced by atmosphere-ocean coupling (Fig. 3) have a positive ΔAPE , with a notable contribution from the lower and middle troposphere (Supplementary Fig. 11). This suggests that the net gain of APE from the sea surface, represented by the reduced APE damping, is key to the increase in ΔKE and, thus, the selective enhancement of circulation variability.

Discussion

The extratropical atmosphere-ocean coupling selectively enhances the three principal modes and 8th mode of atmospheric low-frequency variability while retaining their spatial structure and contributing to their prominence. This selective enhancement occurs because the basin-scale extratropical SST is passive and thus adjustable to large-scale atmospheric anomalies. Our results suggest that the reduction in thermal damping due to the coupling causes a modulation of the energy balance between the dynamical processes inherent in the extratropical atmosphere that determines the structure of the PNA and NAO. As a result, total energy (KE + APE) and, thus, variance of the pattern increase. This process is, therefore, an adjustment rather than a feedback between the atmosphere and the ocean. However, it cannot be explained solely by local thermodynamical adjustment pointed out by

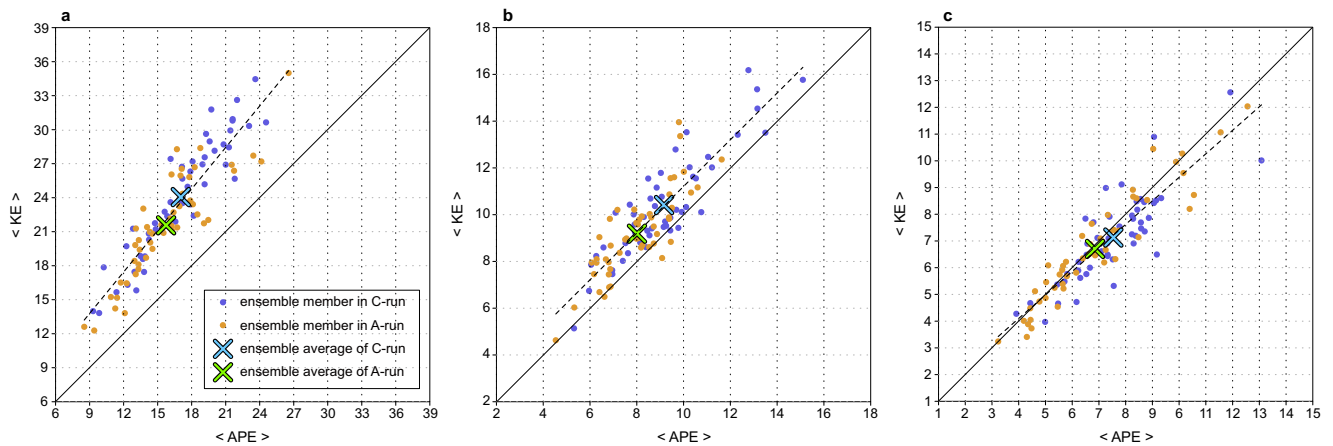


Fig. 10 | Scatter plot of KE and APE for each ensemble member. Scatter plot of KE and APE (units are 10^{17} J) for each ensemble member: EOT1 (a), EOT2 (b), and EOT3 (c). The KE and APE are integrated over the Northern Hemisphere (0° – 360° E, 20° – 90° N) and vertically from the surface to 200hPa. Purple (orange) dots and blue

(green) cross marks indicate each ensemble member in the C-run (A-run) and its ensemble average, respectively. Dashed line indicates linear regression line calculated from all 100 ensemble members without distinction between the C- and A-runs.

previous studies^{31,35–37}. Our results show that the extratropical atmosphere-ocean coupling also involves dynamical adjustment to achieve a mode-specific energy balance.

While the enhancement of the atmospheric low-frequency variability by coupling has also been demonstrated by previous modelling studies, quantitative validity and underlying mechanisms behind this phenomenon remained unclear^{18,41}. For instance, Bladé (1997)³⁵ showed the enhancement of NAO-like variability by comparing perpetual January integrations of an AGCM coupled with a slab ocean mixed-layer model to integrations of the AGCM driven by climatological SST, but local influences from the extratropical ocean dynamics or remote influence from ENSO was not taken into account. By using a similar model configuration, Lau and Nath (1996)³⁴ demonstrated that the extratropical atmosphere-ocean coupling enhances the PNA-like response to ENSO, but there was inconsistency among studies^{39–41} thought to be due to the insufficient sample size⁴¹. Additionally, while the enhancement of surface air temperature variability could be explained by the reduced thermal damping mechanism^{31,35–37}, how the surface coupling enhanced circulation variability throughout the troposphere was not well understood. The present study robustly quantifies the coupling effect based on large ensemble simulations of a state-of-the-art fully coupled model. Moreover, for the first time as we know, it reveals how coupling selectively enhances multiple principal modes of variability, not only thermodynamically but also dynamically.

The adjustable extratropical ocean contributes to the prominence of principal modes of atmospheric low-frequency variability, as the tropical ocean does. However, unlike the tropical ocean, which directly excites the circulation of modes, the extratropical ocean contributes to the persistence of pre-existing circulation anomalies through reduced APE damping. By contrast, recent studies with high-resolution models that can resolve small-scale ocean eddies and sharp oceanic fronts have suggested the active ocean influence on the atmosphere^{19–21}, while our model does not represent such fine-scale processes. In addition, we note that our results do not rule out the existence of atmosphere-ocean positive feedback as argued in previous observational^{32,59} and modelling studies³⁸. It remains an open question of what happens when such active coupling and feedback coexist with the passive coupling argued in this study.

Unravelling what determines the modes enhanced by coupling is a crucial issue. APE changes in the lower and middle troposphere through air-sea coupling are not uniform among the modes. Apparent APE increases are identified only in the three leading modes and 8th mode (Supplementary Fig. 11b), indicating that the reduced APE damping can be effectively

operative only for those modes. Their specific spatial structure, dominant processes of their formation/maintenance and/or their relative positions to midlatitude oceanic frontal zones may determine their susceptibility to the reduced APE damping, but further investigation is needed to clarify the details. Additionally, a larger magnitude of atmospheric circulation anomalies associated with the leading modes may also contribute to the significant coupling effects observed in PNA, NAO, and WACE. The larger their magnitude, the stronger the associated THF (i.e., thermal damping), leading to a larger difference between the C-run and A-run. Therefore, extratropical air-sea coupling contributes to the dominance of PNA, NAO, and WACE.

The WACE pattern is known to be closely related to sea-ice fluctuations in the Barents-Kara Seas in the Arctic^{45,46}. The present results suggest that atmospheric-ocean-sea ice coupling enhances the variance of WACE. Still, it needs to explore further how the atmospheric-ocean-sea ice coupling modulates WACE's energy. Similarly, for the sake of brevity, a detailed analysis for EOT8 (corresponding to NPO^{1,49,50}, Supplementary Fig. 4) cannot be presented in this paper despite the significant coupling effect indicated. Further investigation is warranted in future research.

This study provides robust quantification of the impact of coupling on the variance of atmospheric principal modes by large-ensemble simulations, but the estimates may be dependent on the model used because the model's physical parameterisation determines the damping on APE (i.e., diabatic heating). In addition, there is model bias in the reproducibility of principal modes of low-frequency variability, such as PNA, NAO, and WACE, even in state-of-the-art CGCMs^{47,48}. The reproducibility of those modes and wind variability in the boundary layer⁶⁰ may also affect the quantitative evaluation of the coupling effect. Furthermore, it has been pointed out that models may underestimate the impact of SSTs and sea ice on the atmosphere⁶¹. In fact, our model has a bias where the ocean excessively damped the NAO. Therefore, the actual coupling effects and the signal-to-noise ratio could be greater than our estimates. A more robust estimation of the coupling effect requires continuous improvement of the GCM.

Finally, we emphasise that the APE damping (CQ) in the lower troposphere has a characteristic pattern. This geographically dependent APE damping may indicate the presence of mode-specific sweet spots where the ocean can effectively modulate the behaviour of the mode. Pre-conditioned SST anomalies in the sweet spots may modulate the mode strength and/or the likelihood of mode occurrence by altering the thermal damping efficiency. Much effort is still needed to gain a more comprehensive understanding of the impact of extratropical atmosphere-ocean coupling on

atmospheric low-frequency variability and to make a better prediction and future projection.

Methods

Model experiments

We used the atmosphere-ocean-land coupled GCM, named the sixth version of the Model for Interdisciplinary Research on Climate (MIROC6)⁶². The horizontal resolution of the atmospheric component is a T85 spectral truncation (approximately 1.4° grid interval), and vertically it consists of 81 levels. The model top is 0.004hPa. The ocean component is based on a tripolar coordinate system with 62 vertical levels. The longitudinal grid spacing is 1°, and the meridional grid spacing varies from approximately 0.5° near the equator to 1° in the mid-latitudes.

Based on the protocol of CMIP6⁶³, 50-member ensemble historical simulations⁶⁴ for 1850–2014 and subsequent SSP5–8.5 scenario simulations⁶⁵ for 2015–2100 were conducted. In this study, we used data for the period 1979–2020 from the concatenated two experimental data sets, referred to as the coupled simulation or C-run. The choice of this scenario is very unlikely to affect our results since the difference in scenario forcing is very small at the beginning of the scenario simulation (six years in our analysis).

The 50-member ensemble atmosphere-ocean uncoupled simulation, referred to as the A-run, was also performed by the atmospheric component of the MIROC6 model, which was driven from 1979 to 2020 by external forcings identical to those used in the C-run. The monthly mean SST, sea-ice concentration and thickness fields obtained from the C-run are prescribed in the A-run. For one member of the C-run, we performed one corresponding member of the A-run. Then, adjustments⁶⁶ have been made to the prescribed monthly mean SST and sea-ice values to ensure that the original monthly mean value of the coupled simulation matches exactly with the counterpart in the AGCM after the daily SST and sea-ice fields are linearly interpolated between the prescribed monthly values in AGCM. Therefore, on time scales longer than a month, SST and sea-ice variations are identical between the coupled and corresponding uncoupled simulations. In contrast, the two simulations have different sub-monthly scale variations in SST and sea ice. In AGCM, interpolated daily SST and sea ice vary independently of atmospheric variability, while in CGCM, they fluctuate through interaction with the atmosphere. Variations in sub-monthly scale SST and sea ice tend to be small, and so are the differences in their variance between the two experiments. Therefore, the impact of difference in sub-monthly scale variations, even if amplified by the chaotic nature of the atmospheric circulation, would likely be indistinguishable from vigorous internal variability in the extratropical atmosphere and thus unlikely to be manifested as systematic differences between the two experiments. Therefore, the difference in the long-term statistics of atmospheric variability between coupled and uncoupled simulations can be interpreted as arising from the presence or absence of atmosphere-ocean coupling.

Previous studies using GCM primarily evaluated the coupling effect by comparing AGCM experiments driven by climatological SST and experiments coupling AGCM with a slab ocean model. However, this study designed experiments to ensure that the monthly mean SST and sea ice were identical in CGCM and AGCM. Three reasons support the adoption of this design. Firstly, this experimental configuration allows for significantly reduced differences in the climatological mean states between CGCM and AGCM. The similarity in the climatology between the two experiments eliminates the possibility that the difference in the long-term statistics of atmospheric variability is due to differences in the atmospheric basic state. Secondly, because CGCM includes ocean dynamics, the mid-latitude SST anomaly contains not only atmospheric-driven components but also ocean-driven components. In such a case, it may become challenging to consider the difference from the AGCM experiment driven by climatological SST as a coupling effect directly. Thirdly, it was considered meaningful to demonstrate significant differences in atmospheric low-frequency variability depending on the presence or absence of coupling, even if the monthly mean SST and sea ice were the same in both experiments.

Data

We used a gridded estimate of the observed subsurface ocean temperature⁶⁷ and atmospheric reanalysis data from JRA-55^{68,69}. Variables used include wind velocities (u , v), pressure velocity (ω), temperature (T), geopotential height (Z), diabatic heating rate (Q), surface sea level pressure (SLP), 10 m wind, sensible and latent heat fluxes, sea surface temperature (SST), and sea-ice concentration (SIC). For all these data sets and each model simulation, we defined winter-mean (December, January, February) climatology for 1980–2020 (a year refers to that including January of each DJF season) and anomaly therefrom. Since the monthly-mean SST and SIC are identical in the coupled and uncoupled simulations, the winter-mean climatology of atmospheric fields is virtually identical in the two simulations, and the differences in climatology do not significantly affect the conclusions of this paper.

Statistical test

Statistical tests for correlation/regression coefficients were performed using a two-sided Student's t test, and the variance ratio was tested using a one- or two-sided F -test.

EOT analysis

We applied the EOT analysis^{42,43} to the DJF-mean Z500 anomalies (1980–2020) in JRA-55 and MIROC6 simulations to identify the leading patterns of Northern Hemisphere atmospheric low-frequency variability. The procedure for EOT analysis is as follows (see ref. ⁴² for details). First, multiple one-point regression maps are obtained using every grid point in the analysis domain as a reference grid point. For example, in this study, area-weighted (square root of cosine latitude multiplied) DJF-mean Z500 anomalies in the analysis domain (0°–360°, 20°–90°N) are regressed onto the time series of Z500 anomalies at a reference grid point in the analysis domain. Second, we search for the grid point for which the regression pattern explains the largest amount of temporal variance accumulated in space. The time series of the variable at that grid point and the associated regression pattern are referred to as the first expansion coefficient (EC1) and the first EOT pattern (EOT1), respectively. Next, to create the residual field, the regression anomalies are removed from each grid point and each time step of the original dataset. Then, one-point regression maps are again computed from all grid points to search for the second most dominant pattern. Repeat this procedure to identify higher-order modes. Therefore, variance explained by m -th EOT mode, VAR_m , is calculated from

$$\text{VAR}_m = \sum_{j=1}^S \left\{ \frac{1}{N-1} \sum_{i=1}^N (R_j \alpha_i)^2 \right\} \quad (1)$$

where, α_i is m -th EOT mode's expansion coefficient (EC_m) at a time i ($i = 1, \dots, N$), and R_j is EOT pattern at j -th grid point ($j = 1, \dots, S$) derived from the regression to EC_m . S corresponds to the EOT analysis domain (0°–360°, 20°–90°N).

It is clear from the above procedure, as it is, the EOT patterns are dimensionless, and the ECs have the dimension of the variable. Each EC is standardised in this study, and the original anomaly regressed on the standardised EC is referred to as the EOT pattern. For model simulations, the EOT analysis is applied to a concatenated series of Z500 anomalies (1980–2020) consisting of 100 members, without distinction between the C- and A-runs. Meanwhile, the ECs have been standardised separately; for example, EC1 for the C- and A-runs is referred to as EC1_C and EC1_A , respectively. Therefore, the variance values expressed in Eq. (1) are also calculated separately for the C- and A-runs. Then, anomalies of various physical variables are regressed on the respective standardised EC. Therefore, we should note that the spatial organisation of the EOT pattern is not strictly identical between the C- and A-runs.

For JRA-55, we applied the EOT analysis to a single series of the Z500 anomaly field (1980–2020). Before EOT analysis, Z500 anomalies in JRA-55 are regridded to model T85 resolution for comparison.

Spectral analysis

A spectral analysis was performed on the EC time series, whose variance was weighted to be equal to the explained variance of the mode derived from Eq. (1). The power spectra were obtained after linear detrending and applying a 10 % taper, and a smoothing by 5-point modified Daniell smoothing was applied. The spectra are obtained for each ensemble member and then averaged across the ensemble.

Indices

The EC1, EC2, and EC3 are used as the PNA, NAO, and WACE indices in model simulations. The Niño 3, 3.4, and 4 indices are calculated as the regionally averaged DJF-mean SST anomalies over the eastern (150°W–90°W, 5°S–5°N), central (170°W–120°W, 5°S–5°N), and western (160°E–150°W, 5°S–5°N) equatorial Pacific, respectively.

Energetics of the atmospheric low-frequency variability

For understanding the dynamics governing the generation and maintenance of the pattern of low-frequency variability, it is useful to estimate energy conversion terms^{51,55,58}. In this study, the energetics of the leading modes are compared between the C- and A-runs.

Based on quasi-geostrophic momentum and thermodynamic energy equations in the pressure coordinate system, the growth of kinetic energy (KE) and available potential energy (APE) associated with the low-frequency atmospheric disturbances are given by

$$\frac{\partial}{\partial t} \langle \text{KE} \rangle = \langle \text{CK} \rangle + \langle \text{CK}_{\text{HF}} \rangle + \langle \text{CPK} \rangle \quad (2)$$

$$\frac{\partial}{\partial t} \langle \text{APE} \rangle = \langle \text{CP} \rangle + \langle \text{CP}_{\text{HF}} \rangle - \langle \text{CPK} \rangle + \langle \text{CQ} \rangle \quad (3)$$

with

$$\text{KE} = \frac{u'^2 + v'^2}{2},$$

$$\text{APE} = \gamma^{-1} \frac{T'^2}{2},$$

$$\gamma = \frac{p}{R} \left(\frac{R\hat{T}}{C_p p} - \frac{d\hat{T}}{dp} \right),$$

where γ is a stability parameter, R is the gas constant for dry air (287 J K⁻¹ kg⁻¹), C_p is the specific heat at constant pressure (1004 J K⁻¹ kg⁻¹), and the circumflex denotes an area average over the extratropical Northern Hemisphere (0°–360°E, 20°–90°N). The primes denote deviations from the DJF-mean climatology (denoted as overbars), corresponding to anomalies associated with the three leading modes, PNA, NAO, and WACE, in this study (hereafter mode). The angle brackets denote vertical and hemispheric integration. Energy flux across the tropical boundary is neglected. The terms on the right-hand side of Eqs. (2) and (3) represent the energy conversion terms and are expressed below.

The KE conversion from the climatological DJF-mean flow into the mode is called barotropic energy conversion (CK)⁶ expressed as:

$$\text{CK} = \frac{v'^2 - u'^2}{2} \left(\frac{\partial \bar{u}}{\partial x} - \frac{\partial \bar{v}}{\partial y} \right) - u'v' \left(\frac{\partial \bar{u}}{\partial y} + \frac{\partial \bar{v}}{\partial x} \right) \quad (4)$$

Similarly, the APE conversion from the climatological DJF-mean state into the mode is called baroclinic energy conversion (CP)¹¹ defined as:

$$\text{CP} = -\gamma^{-1} \left(u'T' \frac{\partial \bar{T}}{\partial x} + v'T' \frac{\partial \bar{T}}{\partial y} \right) \quad (5)$$

In addition, the diabatic APE generation term acts as the source or sink of the APE, which is evaluated as:

$$\text{CQ} = \gamma^{-1} \frac{Q'T'}{C_p} \quad (6)$$

Energy conversion from APE to KE is expressed as:

$$\text{CPK} = -\frac{R\omega'T'}{p} \quad (7)$$

which appears in Eqs. (2) and (3) with the opposite sign.

Finally, the KE and APE transfer via feedback forcing by high-frequency transient eddies to the DJF-mean anomalies^{7,9} are defined as:

$$\text{CK}_{\text{HF}} = -u' \left\{ \frac{\partial}{\partial x} (u''u'')' + \frac{\partial}{\partial y} (u''v'')' \right\} - v' \left\{ \frac{\partial}{\partial x} (u''v'')' + \frac{\partial}{\partial y} (v''v'')' \right\} \quad (8)$$

$$\text{CP}_{\text{HF}} = -\gamma^{-1} T' \left\{ \frac{\partial}{\partial x} (u''T'')' + \frac{\partial}{\partial y} (v''T'')' \right\} \quad (9)$$

where the double primes denote 10-day high-pass-filtered fluctuations associated with transient eddies. CK_{HF} and CP_{HF} are called barotropic feedback and baroclinic feedback, respectively⁵¹.

In comparing the energetics of the mode between the C- and A-runs, it should be noted that the C-run yields larger energy than the A-run. For a fair comparison, all the energy conversion terms in Eqs. (2) and (3) are divided by the total energy ($\langle \text{KE} \rangle + \langle \text{APE} \rangle$) of the mode. The resultant value is called efficiency (denoted as asterisk) because its inverse represents the time scale over which a given process alone could fully replenish the total energy, and it is independent of the magnitude of the pattern associated with the mode^{55,58}.

In this study, the anomalies of the variables regressed onto the EOT indices are used to calculate each conversion term without distinguishing the polarity of the mode. All terms in Eqs. (2) and (3) are integrated over the extratropical Northern Hemisphere (0°–360°E, 20°–90°N) and vertically from the surface up to 200hPa. Due to the limited available data for the diabatic heating rate (Q), calculations for CQ were made using only ten ensemble members from 1979–2013 for each C- and A-runs. The Q is the sum of the diabatic heating terms from different physical processes in the model, which include vertical diffusion, cumulus heating, large-scale condensation heating, shallow convection heating, cloud physics heating, and radiative heating by long wave and short wave. Hence, CQ term is also decomposed into contributions from the respective physical processes (Supplementary Figs. 8 and 9). We have confirmed that the differences in the climatological mean state between the C- and A-runs do not significantly affect the result of energetics.

Data availability

The gridded estimate of the observed subsurface ocean temperature⁶⁷ is available from <https://climate.mri-jma.go.jp/pub/archives/Ishii-et-al-Ocean-Subsurface-TS-v7.2/>, and the JRA-55 data sets^{68,69} is available from https://jra.kishou.go.jp/JRA-55/index_en.html. The MIROC6 historical and SSP5-8.5 scenario simulations are available from the Earth System Grid Federation (ESGF) archive (<https://esgf-node.lln.gov/search/cmip6/>). The MIROC6 AGCM data used in this study⁷⁰ are available from <https://doi.org/10.5281/zenodo.10565870>. The data files for producing the charts and graphs of this manuscript are deposited in the public repository (<https://doi.org/10.5281/zenodo.10570690>).

Code availability

The Fortran codes used for the analysis are available upon request from the corresponding author.

Received: 20 September 2023; Accepted: 21 February 2024;

Published online: 15 March 2024

References

- Wallace, J. M. & Gutzler, D. S. Teleconnections in the geopotential height field during the Northern Hemisphere winter. *Mon Weather Rev.* **109**, 784–812 (1981).
- Barnston, A. G. & Livezey, R. E. Classification, seasonality and persistence of low-frequency atmospheric circulation patterns. *Mon. Weather Rev.* **115**, 1083–1126 (1987).
- Marshall, J. et al. North Atlantic climate variability: phenomena, impacts and mechanisms. *Int. J. Climatol.* **21**, 1863–1898 (2001).
- Yeh, S. W. et al. ENSO atmospheric teleconnections and their response to greenhouse gas forcing. *Rev. Geophys.* **56**, 185–206 (2018).
- Hurrell, J. W., Kushnir, Y., Ottersen, G. & Visbeck, M. An overview of the North Atlantic oscillation. *The North Atlantic Oscillation: climatic significance and environmental impact*, 1–35 (2003).
- Simmons, A., Wallace, J. & Branstator, G. Barotropic wave propagation and instability, and atmospheric teleconnection patterns. *J. Atmos. Sci.* **40**, 1363–1392 (1983).
- Lau, N.-C. & Holopainen, E. O. Transient eddy forcing of the time-mean flow as identified by geopotential tendencies. *J. Atmos. Sci.* **41**, 313–328 (1984).
- Branstator, G. Analysis of general circulation model sea-surface temperature anomaly simulations using a linear model. Part I: Forced solutions. *J. Atmos. Sci.* **42**, 2225–2241 (1985).
- Lau, N.-C. Variability of the observed midlatitude storm tracks in relation to low-frequency changes in the circulation pattern. *J. Atmos. Sci.* **45**, 2718–2743 (1988).
- Held, I. M., Lyons, S. W. & Nigam, S. Transients and the extratropical response to El Niño. *J. Atmos. Sci.* **46**, 163–174 (1989).
- Branstator, G. Low-frequency patterns induced by stationary waves. *J. Atmos. Sci.* **47**, 629–649 (1990).
- Lau, N.-C. A diagnostic study of recurrent meteorological anomalies appearing in a 15-year simulation with a GFDL general circulation model. *Mon. Weather Rev.* **109**, 2287–2311 (1981).
- Delworth, T. L. North Atlantic interannual variability in a coupled ocean–atmosphere model. *J. Clim.* **9**, 2356–2375 (1996).
- Trenberth, K. E. et al. Progress during TOGA in understanding and modeling global teleconnections associated with tropical sea surface temperatures. *J. Geophys. Res.: Oceans* **103**, 14291–14324 (1998).
- Mori, M. & Watanabe, M. The growth and triggering mechanisms of the PNA: A MJO-PNA coherence. *J. Meteorol. Soc. Jpn.* **86**, 213–236 (2008).
- Abid, M. A. et al. Separating the Indian and Pacific Ocean impacts on the Euro-Atlantic response to ENSO and its transition from early to late winter. *J. Clim.* **34**, 1531–1548 (2021).
- Frankignoul, C. Sea surface temperature anomalies, planetary waves, and air–sea feedback in the middle latitudes. *Rev. Geophys.* **23**, 357–390 (1985).
- Kushnir, Y. et al. Atmospheric GCM response to extratropical SST anomalies: Synthesis and evaluation. *J. Clim.* **15**, 2233–2256 (2002).
- Czaja, A., Frankignoul, C., Minobe, S. & Vannière, B. Simulating the midlatitude atmospheric circulation: what might we gain from high-resolution modeling of air–sea interactions? *Curr. Clim. Change Rep.* **5**, 390–406 (2019).
- Kwon, Y.-O. et al. Role of the Gulf Stream and Kuroshio–Oyashio systems in large-scale atmosphere–ocean interaction: A review. *J. Clim.* **23**, 3249–3281 (2010).
- Seo, H. et al. Ocean mesoscale and frontal-scale ocean–atmosphere interactions and influence on large-scale climate: A review. *J. Clim.* **36**, 1981–2013 (2023).
- Cayan, D. R. Latent and sensible heat flux anomalies over the northern oceans: Driving the sea surface temperature. *J. Phys. Oceanogr.* **22**, 859–881 (1992).
- Cayan, D. R. Latent and sensible heat flux anomalies over the northern oceans: The connection to monthly atmospheric circulation. *J. Clim.* **5**, 354–369 (1992).
- Alexander, M. A. & Scott, J. D. Surface flux variability over the North Pacific and North Atlantic oceans. *J. Clim.* **10**, 2963–2978 (1997).
- Seager, R. et al. Causes of Atlantic Ocean climate variability between 1958 and 1998. *J. Clim.* **13**, 2845–2862 (2000).
- Marshall, J., Johnson, H. & Goodman, J. A study of the interaction of the North Atlantic Oscillation with ocean circulation. *J. Clim.* **14**, 1399–1421 (2001).
- Visbeck, M. et al. The ocean’s response to North Atlantic Oscillation variability. *Geophys. Monogr.-Am. Geophys. Union* **134**, 113–146 (2003).
- Alexander, M. A. & Scott, J. D. The role of Ekman ocean heat transport in the Northern Hemisphere response to ENSO. *J. Clim.* **21**, 5688–5707 (2008).
- Barsugli, J. J. *Idealized models of intrinsic midlatitude atmosphere–ocean interaction*, University of Washington, (1995).
- Chang, P., Richter, I., Dijkstra, H., Wieners, C. & Myers, T. Atmosphere–ocean interactions. in *Interacting Climates of Ocean Basins: Observations, Mechanisms, Predictability, and Impacts* 89–119 (Cambridge: Cambridge University Press., 2020).
- Barsugli, J. J. & Battisti, D. S. The basic effects of atmosphere–ocean thermal coupling on midlatitude variability. *J. Atmos. Sci.* **55**, 477–493 (1998).
- Czaja, A., Robertson, A. W. & Huck, T. The role of Atlantic ocean–atmosphere coupling in affecting North Atlantic oscillation variability. *Geophys. Monogr. Ser.* **134**, 147–172 (2003).
- Manabe, S. & Stouffer, R. J. Low-frequency variability of surface air temperature in a 1000-year integration of a coupled atmosphere–ocean–land surface model. *Journal of Climate* **9**, 376–393 (1996).
- Lau, N.-C. & Nath, M. J. The role of the “atmospheric bridge” in linking tropical Pacific ENSO events to extratropical SST anomalies. *Journal of Climate* **9**, 2036–2057 (1996).
- Bladé, I. The influence of midlatitude ocean–atmosphere coupling on the low-frequency variability of a GCM. Part I: no tropical SST forcing*. *J. Clim.* **10**, 2087–2106 (1997).
- Bhatt, U. S., Alexander, M. A., Battisti, D. S., Houghton, D. D. & Keller, L. M. Atmosphere–ocean interaction in the North Atlantic: Near-surface climate variability. *J. Clim.* **11**, 1615–1632 (1998).
- Saravanan, R. Atmospheric low-frequency variability and its relationship to midlatitude SST variability: Studies using the NCAR climate system model. *J. Clim.* **11**, 1386–1404 (1998).
- Watanabe, M. & Kimoto, M. Atmosphere–ocean thermal coupling in the North Atlantic: A positive feedback. *Quart. J. R. Meteorol. Soc.* **126**, 3343–3369 (2000).
- Bladé, I. The influence of midlatitude ocean–atmosphere coupling on the low-frequency variability of a GCM. Part II: Interannual variability induced by tropical SST forcing. *J. Clim.* **12**, 21–45 (1999).
- Lau, N.-C. & Nath, M. J. Impact of ENSO on SST variability in the North Pacific and North Atlantic: Seasonal dependence and role of extratropical sea–air coupling. *J. Clim.* **14**, 2846–2866 (2001).
- Alexander, M. A. et al. The atmospheric bridge: The influence of ENSO teleconnections on air–sea interaction over the global oceans. *J. Clim.* **15**, 2205–2231 (2002).
- Van den Dool, H., Saha, S. & Johansson, Å. Empirical orthogonal teleconnections. *J. Clim.* **13**, 1421–1435 (2000).
- Smoliak, B. V. & Wallace, J. M. On the leading patterns of Northern Hemisphere sea level pressure variability*. *J. Atmos. Sci.* **72**, 3469–3486 (2015).

44. Thompson, D. W. & Wallace, J. M. Annular modes in the extratropical circulation. Part I: month-to-month variability*. *J. Clim.* **13**, 1000–1016 (2000).
45. Mori, M., Watanabe, M., Shiogama, H., Inoue, J. & Kimoto, M. Robust Arctic sea-ice influence on the frequent Eurasian cold winters in past decades. *Nat. Geosci.* **7**, 869–873 (2014).
46. Mori, M., Kosaka, Y., Watanabe, M., Nakamura, H. & Kimoto, M. A reconciled estimate of the influence of Arctic sea-ice loss on recent Eurasian cooling. *Nat. Clim. Change* **9**, 123–129 (2019).
47. Lee, J., Sperber, K. R., Gleckler, P. J., Bonfils, C. J. & Taylor, K. E. Quantifying the agreement between observed and simulated extratropical modes of interannual variability. *Clim. Dyn.* **52**, 4057–4089 (2019).
48. Eyring, V. et al. Human influence on the climate system. in *Climate Change 2021: The Physical Science Basis. Contribution of Working Group I to the Sixth Assessment Report of the Intergovernmental Panel on Climate Change*, 423–552 (2021).
49. Linkin, M. E. & Nigam, S. The North Pacific Oscillation–west Pacific teleconnection pattern: Mature-phase structure and winter impacts. *J. Clim.* **21**, 1979–1997 (2008).
50. Chen, S. & Wu, R. Impacts of winter NPO on subsequent winter ENSO: Sensitivity to the definition of NPO index. *Clim. Dyn.* **50**, 375–389 (2018).
51. Tanaka, S., Nishii, K. & Nakamura, H. Vertical structure and energetics of the western Pacific teleconnection pattern. *J. Clim.* **29**, 6597–6616 (2016).
52. Aru, H., Chen, S. & Chen, W. Comparisons of the different definitions of the western Pacific pattern and associated winter climate anomalies in Eurasia and North America. *Int. J. Climatol.* **41**, 2840–2859 (2021).
53. Feldstein, S. B. The timescale, power spectra, and climate noise properties of teleconnection patterns. *J. Clim.* **13**, 4430–4440 (2000).
54. Deser, C., Alexander, M. A., Xie, S.-P. & Phillips, A. S. Sea surface temperature variability: Patterns and mechanisms. *Ann. Rev. Marine Sci.* **2**, 115–143 (2010).
55. Martineau, P., Nakamura, H., Kosaka, Y. & Yamamoto, A. Importance of a vertically tilting structure for energizing the North Atlantic Oscillation. *Sci. Rep.* **10**, 1–10 (2020).
56. Barnes, E. A. & Hartmann, D. L. Dynamical feedbacks and the persistence of the NAO. *J. Atmos. Sci.* **67**, 851–865 (2010).
57. Kim, M., Yoo, C., Sung, M.-K. & Lee, S. Classification of wintertime atmospheric teleconnection patterns in the Northern Hemisphere. *J. Clim.* **34**, 1847–1861 (2021).
58. Kosaka, Y., Nakamura, H., Watanabe, M. & Kimoto, M. Analysis on the dynamics of a wave-like teleconnection pattern along the summertime Asian jet based on a reanalysis dataset and climate model simulations. *J. Meteorol. Soc. Jpn.* **87**, 561–580 (2009).
59. Czaja, A. & Frankignoul, C. Observed impact of Atlantic SST anomalies on the North Atlantic Oscillation. *J. Clim.* **15**, 606–623 (2002).
60. Sura, P. & Newman, M. The impact of rapid wind variability upon air-sea thermal coupling. *J. Clim.* **21**, 621–637 (2008).
61. Scaife, A. A. & Smith, D. A signal-to-noise paradox in climate science. *npj Clim. Atmos. Sci.* **1**, 28 (2018).
62. Tatebe, H. et al. Description and basic evaluation of simulated mean state, internal variability, and climate sensitivity in MIROC6. *Geosci. Model Dev.* **12**, 2727–2765 (2019).
63. Eyring, V. et al. Overview of the Coupled Model Intercomparison Project Phase 6 (CMIP6) experimental design and organization. *Geosci. Model Dev.* **9**, 1937–1958 (2016).
64. Tatebe, H. & Watanabe, M. MIROC MIROC6 model output prepared for CMIP6 CMIP. *Earth Syst. Grid Federation* <https://doi.org/10.22033/ESGF/CMIP6.5603> (2018).
65. Shiogama, H., Abe, M. & Tatebe, H. MIROC MIROC6 model output prepared for CMIP6 ScenarioMIP ssp585. *Earth Syst. Grid Federation* <https://doi.org/10.22033/ESGF/CMIP6.5771> (2019).
66. Taylor, K., Williamson, D. & Zwiers, F. The sea surface temperature and sea-ice concentration boundary conditions for AMIP II simulations, PCMDI Rep. 60, 25 pp. *Program for Clim. Model Diagn. and Intercompar., Lawrence Livermore Natl. Lab., Livermore, Ca* (2000).
67. Ishii, M. et al. Accuracy of global upper ocean heat content estimation expected from present observational data sets. *Sola* **13**, 163–167 (2017).
68. Kobayashi, S. et al. The JRA-55 reanalysis: General specifications and basic characteristics. *J. Meteorol. Soc. Jpn. Ser. II* **93**, 5–48 (2015).
69. Harada, Y. et al. The JRA-55 Reanalysis: Representation of atmospheric circulation and climate variability. *J. Meteorol. Soc. Jpn. Ser. II* **94**, 269–302 (2016).
70. Mori, M. MIROC6-AGCM dataset for “Northern Hemisphere winter atmospheric teleconnections are intensified by extratropical ocean-atmosphere coupling”. <https://doi.org/10.5281/zenodo.10565870>.

Acknowledgements

We thank three anonymous reviewers for their helpful comments. This work is supported by the Japan Ministry of Education, Culture, Sports, Science and Technology through the advanced studies of climate change projection (SENTAN: Grant Number JPMXD0722680395) Program, the Arctic Challenge for Sustainability II (ArCS II: Grant Number JPMXD1420318865) Program, by the Japan Society for the Promotion of Science through KAKENHI Grant Number JP19H05701, JP19H05702, JP19H05703, JP19H05704, JP20H01970, JP22H01292, JP22H01299, JP23H01241, JP23H01250, by the Japanese Ministry of Environment through Environment Research and Technology Development Fund JPMEERF20222002 and by the Japan Science and Technology Agency through COI-NEXT JPMJPF2013.

Author contributions

M.M. designed the research. M.M. and H.Tatebe performed the numerical experiments. M.M. performed the analyses and wrote the manuscript with discussion and feedback from Y.K, B.T, H.Tokina, H.Tatebe, and H.N.

Competing interests

The authors declare no competing interests.

Additional information

Supplementary information The online version contains supplementary material available at <https://doi.org/10.1038/s43247-024-01282-1>.

Correspondence and requests for materials should be addressed to Masato Mori.

Peer review information *Communications Earth & Environment* thanks Sang-Wook Yeh, Michael Alexander and the other, anonymous, reviewer(s) for their contribution to the peer review of this work. Primary Handling Editors: Kyung-Sook Yun and Aliénor Lavergne. A peer review file is available.

Reprints and permissions information is available at <http://www.nature.com/reprints>

Publisher's note Springer Nature remains neutral with regard to jurisdictional claims in published maps and institutional affiliations.

Open Access This article is licensed under a Creative Commons Attribution 4.0 International License, which permits use, sharing, adaptation, distribution and reproduction in any medium or format, as long as you give appropriate credit to the original author(s) and the source, provide a link to the Creative Commons licence, and indicate if changes were made. The images or other third party material in this article are included in the article's Creative Commons licence, unless indicated otherwise in a credit line to the material. If material is not included in the article's Creative Commons licence and your intended use is not permitted by statutory regulation or exceeds the permitted use, you will need to obtain permission directly from the copyright holder. To view a copy of this licence, visit <http://creativecommons.org/licenses/by/4.0/>.

© The Author(s) 2024